

# Surface engineered carbon quantum dots for efficient photocatalytic hydrogen peroxide production

Wenyuan Han<sup>a,b</sup>, Hao Zhang<sup>a</sup>, Degang Li<sup>a,\*</sup>, Wenwu Qin<sup>b</sup>, Xuliang Zhang<sup>a</sup>, Shaobin Wang<sup>c</sup>, Xiaoguang Duan<sup>c,\*</sup>

<sup>a</sup> School of Chemistry and Chemical Engineering, Shandong University of Technology, Zibo 255000, PR China

<sup>b</sup> Key Laboratory of Nonferrous Metal Chemistry and Resources Utilization of Gansu Province, State Key Laboratory of Applied Organic Chemistry and Key Laboratory of Special Function Materials and Structure Design (MOE), College of Chemistry and Chemical Engineering, Lanzhou University, Lanzhou 730000, PR China

<sup>c</sup> School of Chemical Engineering, The University of Adelaide, Adelaide, SA 5005, Australia



## ARTICLE INFO

### Keywords:

Carbon quantum dots  
Oxygen reduction  
Photocatalysis  
Hydrogen peroxide  
Proton coupled electron transfer

## ABSTRACT

Photocatalytic production of hydrogen peroxide ( $H_2O_2$ ) from  $O_2$  and water offers a sustainable and environmentally friendly approach to solar-to-chemical energy conversion. To address the low  $H_2O_2$  yield of pristine carbon quantum dots (CQDs) ( $354 \mu\text{mol g}^{-1} \text{ h}^{-1}$ ), we applied molecular level engineering of CQDs through surface NH functionalization (CQDs-NH), which significantly increased photocatalytic activity of  $H_2O_2$  production to  $2974 \mu\text{mol g}^{-1} \text{ h}^{-1}$ . This enhanced performance is attributed to the  $\text{C}=\text{N}-\text{NH}-$  group in CQDs-NH, which improves light absorption, facilitates carrier separation and transfer, increases the selectivity of two-electron oxygen reduction reaction, and promotes oxygen adsorption. Additionally, the hydrogen atom in the  $\text{C}=\text{N}-\text{NH}-$  group acts as a proton conductor, which significantly promoted the proton-coupled electron transfer process to produce  $H_2O_2$  in the presence of  $O_2$ . Moreover, a high  $H_2O_2$  production capacity of  $2764 \mu\text{mol g}^{-1} \text{ h}^{-1}$  was obtained even in the absence of an electron donor.

## 1. Introduction

Hydrogen peroxide ( $H_2O_2$ ), a vital green oxidant, has been extensively used in various fields, including textile printing and dyeing, chemical industry, environmental treatment, biomedicine, and chemical synthesis [1,2]. Given the increasing demand for sustainable energy,  $H_2O_2$  has emerged as a promising chemical fuel, offering higher energy density and zero emissions compared to compressed  $H_2$  gas [3,4]. However, large-scale  $H_2O_2$  production still largely relies on the conventional anthraquinone-based method, which requires expensive precious metal catalysts, involves high energy consumption, and uses toxic organic solvents [5–7]. Consequently, developing a safe, energy-efficient, and environmentally friendly strategy for  $H_2O_2$  production is of paramount importance.

Electrocatalytic and photocatalytic  $H_2O_2$  generation have emerged as promising alternatives to the conventional anthraquinone process, offering environmental friendliness and sustainability [8–10]. Unlike the severe energy consumption associated with electrocatalytic methods and the challenges in the low activity/selectivity in coordinating the two

electron transfer pathway in oxygen reduction reactions (ORR), photocatalytic reactions can effectively convert solar energy into chemical energy. This process involves capturing sunlight under mild conditions and driving semiconductors to produce  $H_2O_2$  from dissolved oxygen. The energy band structure of semiconductor photocatalysts allows for the generation of highly reactive electron-hole pairs excited by photons [11,12]. The high-energy photogenerated holes and electrons will separately migrate to the catalyst surface and engage in oxidation/reduction reactions with adsorbed reactant molecules [13–16].

Carbon quantum dots (CQDs), as emerging metal-free photosensitive nanomaterials, have garnered significant research interest due to their unique properties, including ease of preparation, environmental friendliness, functionalizability, and suitable energy band structures to coordinate diverse redox reactions [17–19]. CQDs have found wide application in various photocatalytic endeavors, such as pollutant degradation [20–22], water decomposition [23,24],  $CO_2$  reduction [25–27],  $N_2$  fixation [28,29], and  $H_2O_2$  production [30–32]. However, their performance in photocatalytic  $H_2O_2$  generation is hindered by limited light absorption, high electron-hole recombination rate, slow

\* Corresponding authors.

E-mail addresses: [ldg@sdut.edu.cn](mailto:ldg@sdut.edu.cn) (D. Li), [Xiaoguang.duan@adelaide.edu.au](mailto:Xiaoguang.duan@adelaide.edu.au) (X. Duan).

charge carrier transfer rates, lower selectivity for two-electron ORR, and weak surface oxygen adsorption capacity[33,34]. Various strategies have been proposed to overcome these inherent limitations of CQDs, including the introduction of defects [35], heteroatom doping [36,37], construction of heterojunctions [38], and hybridization with carbon materials [39]. These strategies have improved photocatalytic performance by extending the light absorption range and enhancing the separation and transfer of photogenerated carriers. However, the strategies mentioned above often involve complex preparation processes and/or require harsh reaction conditions. Consequently, there is a pressing need for a rapid and straightforward method to improve the photocatalytic efficiency of CQDs. The surface of CQDs can be rationally designed under simple reaction conditions (ambient temperature, atmospheric pressure, and without the need for a catalyst) to enhance their photocatalytic activity. The multiple functional groups on their surface can serve as excellent platforms for molecular assembly. Yan et al. leveraged a condensation reaction between carboxyl and amino groups to attach a series of electron-donating groups at the edges of the carbon dot conjugate structure [40]. They introduced intermediate n orbitals between  $\pi$  and  $\pi^*$  orbitals to narrow the bandgap, significantly boosting the photocatalytic water splitting and CO<sub>2</sub> reduction activities of graphene quantum dots. Similarly, Gu et al. developed CQDs-AQ by modifying the surface of CQDs with anthraquinone (AQ) molecules, utilizing AQ as a co-catalyst to promote efficient carrier separation and accelerate the two-electron ORR pathway [41].

In this study, we report the design and synthesis of a novel and efficient metal-free quantum photocatalyst based on the Schiff base condensation reaction. We systematically investigate the effect of NH group introduction on promoting photocatalytic H<sub>2</sub>O<sub>2</sub> generation. Experiments and density functional theory (DFT) calculations show that the C=N-NH- group in CQDs-NH enhances light absorption, facilitates carrier separation/transfer, and oxygen adsorption. It also promotes the formation of the critical intermediate species (\*OOH), thus significantly improving the selectivity and activity of H<sub>2</sub>O<sub>2</sub> production. Due to the unique photoelectron and proton donating ability of CQDs-NH, high hydrogen peroxide yields have been achieved in the presence and absence of sacrificial agents. Our study offers new strategy for the design of metal-free carbon-based photocatalysis for efficient H<sub>2</sub>O<sub>2</sub> generation and other photocatalytic applications.

## 2. Materials and methods

### 2.1. Chemicals

Glucose, hydrogen peroxide (H<sub>2</sub>O<sub>2</sub>, 30 wt%) aqueous solution, ethanol (EA, 99.9%), sodium hydroxide (NaOH, 98%), sulfuric acid (H<sub>2</sub>SO<sub>4</sub>), silver nitrate (SN, 99%), Tetrabutylammonium Perchlorate (TBAP, 99%), and ethylenediaminetetraacetic acid disodium salt (EDTA-2Na, 99%) were procured from Sinopharm Chemical Reagent Co. Ltd. (Shanghai, China). Potassium dihydrogen phosphate (KH<sub>2</sub>PO<sub>4</sub>, 99.5%), potassium hydrogen phosphate (K<sub>2</sub>HPO<sub>4</sub>, 99%), dichloromethane (CHCl<sub>2</sub>), phenylamine (PA, 99%), phenyl hydrazine (PH, 99%),  $\beta$ -naphthylamine (NA, 97%), 2-naphthylhydrazine (NH, 98%), p-benzoquinone (BQ, 99%), and tert-butanol (TBA, 99%) were obtained from Adamas Reagent Co. Ltd. (Shanghai, China). N, N-diethyl-p-phenylenediamine (DPD, 98%) and peroxidase from horseradish (POD, activity: >200 units mg<sup>-1</sup>) were sourced from Aladdin Reagent Co. Ltd. (Shanghai, China). All chemicals were used as received without further purification.

### 2.2. Synthesis of CQDs and CQDs-derivatives

CQDs were synthesized through a one-step pyrolysis reaction of glucose and hydrogen peroxide. Specifically, 2 g of glucose was dissolved in 4 mL of hydrogen peroxide solution, then the mixture was transferred to a glass petri dish and carbonized at 200 °C for 20 min. The

brown solid obtained was prepared into a 10 mg/mL aqueous solution and dialyzed in deionized water for 72 h (500 MWCO) to remove impurities. After dialysis, the solution was freeze-dried to yield CQDs powder.

CQDs-derivatives were synthesized by chemically titrating aldehyde carbonyls on the CQDs' surface through a Schiff-base condensation reaction. The detailed procedure is described in [Text S1](#). The derivatives derived from PA, PH, NA, and NH are labeled as CQDs-PA, CQDs-PH, CQDs-NA, and CQDs-NH, respectively.

### 2.3. Characterization

Characterization of the samples involved several techniques. Transmission Electron Microscopy (TEM) and High-Resolution TEM (HRTEM) analyses were conducted using a FEI Tecnai G2 F20 S-TWIN TEM operating at 200 kV. Raman spectra were acquired with a LabRAM HR800 spectrometer utilizing a 532 nm laser source. Additionally, Fourier-transform Infrared (FT-IR) spectra were recorded using a Bruker Tensor-II, employing the KBr pellet technique. X-ray Diffraction (XRD) patterns were collected on an Ultima IV diffractometer with a Cu K $\alpha$  radiation source ( $\lambda = 0.154$  nm), and X-ray Photoelectron Spectroscopy (XPS) analysis was conducted on a Kratos Axis UltraDLD spectrometer using Al K $\alpha$  radiation ( $h\nu = 1486.6$  eV). The UV-Vis absorption spectra were recorded on a Shimadzu UV-2450PC spectrophotometer equipped with an integrating sphere. Photoluminescence (PL) spectra were recorded using a Hitachi F-4600 luminescence spectrometer. For Electron Paramagnetic Resonance (EPR) spectra, a Bruker EPR JES-FA200 spectrometer was employed, equipped with a BoPhilae PLS-SXE300DUV 300 W Xe lamp and an AM 1.5 G filter (100 mW/cm<sup>2</sup>) as the light source.

### 2.4. Electrochemical measurement

Photoelectrochemical tests were conducted using a standard three-electrode system with a platinum wire and a saturated calomel electrode (SCE) as counter and reference electrodes, respectively. The as-prepared CQDs and CQDs-derivatives were immobilized on a glassy carbon electrode as the working electrode. The electrolyte was a 0.5 M Na<sub>2</sub>SO<sub>4</sub> solution. The working electrode was irradiated with visible light from a 300 W Xe lamp with an AM 1.5 G filter (100 mW/cm<sup>2</sup>). Mott-Schottky experiments were carried out at 1.5 kHz frequencies. Chopped-light amperometric I-t characterization is conducted using repetitive light-dark cycles. Cyclic voltammetry (CV) was used to assess the relationship between response current and potential. Electrochemical impedance spectroscopy (EIS) was performed at open circuit potentials and frequencies ranging from 0.1 Hz to 100 kHz. Rotating ring disk electrode (RRDE) analyses were conducted by linearly sweeping the disk potential from -1.0–0.0 V vs. Ag/AgCl (4 M KCl) in O<sub>2</sub>-saturated 0.1 M KOH electrolyte at different rotation rates ranging from 100 to 2500 rpm. The electron transfer number (n) and H<sub>2</sub>O<sub>2</sub> selectivity were calculated using the disk current (I<sub>d</sub>) and ring current (I<sub>r</sub>) results according to the following equations:

$$n = \frac{4 \times I_d}{I_d + I_r/N} \times 100\% \quad (1)$$

$$H_2O_2(\%) = \frac{I_r/N}{I_d + I_r/N} \times 200\% \quad (2)$$

where I<sub>r</sub> is the ring current, I<sub>d</sub> is the disk current, and N is the collection efficiency (0.428) of the RRDE.

### 2.5. In-situ ATR-FTIR spectroscopy

In-situ ATR-FTIR spectrometer were performed using a Thermo Nicolet iS50 FT-IR spectrometer equipped with a diamond internal

reflection element (IRE) to probe the surface groups of CQDs-NH. Briefly, 10  $\mu$ L of 5 mg/mL CQDs-NH solution was dropped onto the diamond IRE and dried to form CQDs-NH film under an inert atmosphere [42]. The film was equilibrated with an O<sub>2</sub>-saturated aqueous solution under O<sub>2</sub> atmosphere, and the background spectra were recorded simultaneously. For the in-situ FT-IR analysis experiments, the changes in the infrared spectra of the film were recorded during

irradiation using a 300 W Xe lamp with AM 1.5 G filter (100 mW/cm<sup>2</sup>).

## 2.6. Photocatalytic experiments

Photocatalytic H<sub>2</sub>O<sub>2</sub> production was evaluated by using a 300 W Xe lamp with AM 1.5 G filter (100 mW/cm<sup>2</sup>). Specifically, 10 mg of catalyst was dispersed into a glass reactor containing 50 mL of 10% ethanol

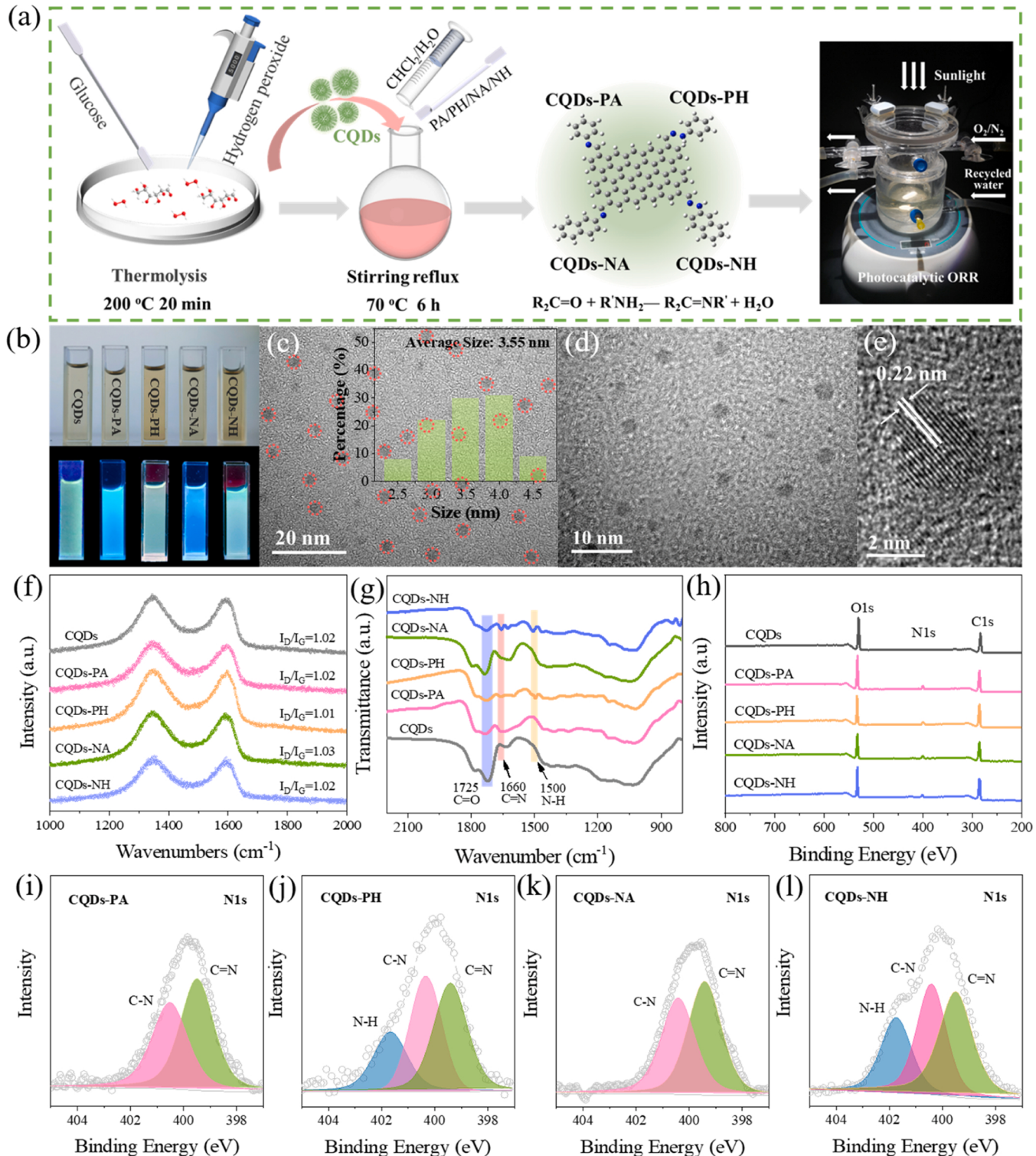


**Fig. 1.** (a) Schematic diagram of the preparation of CQDs and CQDs-derivatives. (b) The photographs of CQDs and CQDs-derivatives under visible and 365 nm UV illumination. (c, d) HRTEM and particle size distribution images for CQDs-NH. (e) The HRTEM images of CQDs-NH with high magnification. (f) Raman spectra, (g) FT-IR spectra, (h) XPS survey scans of CQDs and CQDs-derivatives. (i-l) N1s XPS spectra of CQDs-derivatives.

solution. All the reaction system was kept at 25 °C as controlled by cooling water. Then, after starting illumination, 2 mL of the reaction solution was removed from the reaction system at regular intervals. The DPD colorimetric method was used to measure the concentration of H<sub>2</sub>O<sub>2</sub> produced, and the details were presented in Text S2. All experiments were conducted under atmospheric conditions unless otherwise stated.

### 2.7. Computational methods

Density functional theory (DFT) calculations were performed using Gaussian 16 C.01 software. To explore intramolecular interactions, 20 initial candidate conformations were generated and optimized using specific computational methods. Additionally, all wave function analyses were performed using Multiwfn 3.8 software [43]. The calculation details were given in SI (Text S3).

## 3. Results and discussions

### 3.1. Structural characterization

As depicted in Fig. 1a, CQDs were synthesized via a one-step pyrolysis process using glucose and hydrogen peroxide as the precursor and carbonization agents, respectively. Subsequently, a series of CQDs derivatives were generated by reacting with carbonyl groups on the CQDs surface, utilizing different ligands through Schiff-base condensation. Fig. 1b illustrates that all five carbon dot variants emit distinct fluorescence under UV light irradiation. Notably, CQDs-PA and CQDs-NA exhibit cyan blue fluorescence, in contrast to CQDs, CQDs-PH, and CQDs-NH. High-resolution transmission electron microscopy (HRTEM) reveals that both CQDs and CQDs-NH are well dispersed, with a lateral size distribution ranging from 2 to 5 nm (Fig. 1c, d, Fig. S1). The average size of CQDs-NH (3.55 nm) is slightly larger than that of CQDs (3.21 nm). CQDs-NH displays a typical ellipsoidal shape with a lattice spacing of 0.22 nm, corresponding to the graphene (100) plane (Fig. 1e) [44]. Raman spectra of both CQDs and their derivatives display typical D and G bands at 1345 cm<sup>-1</sup> and 1590 cm<sup>-1</sup> for defective and sp<sup>2</sup>-hybridized carbons, respectively (Fig. 1f) [45]. The similar I<sub>D</sub>/I<sub>G</sub> values across

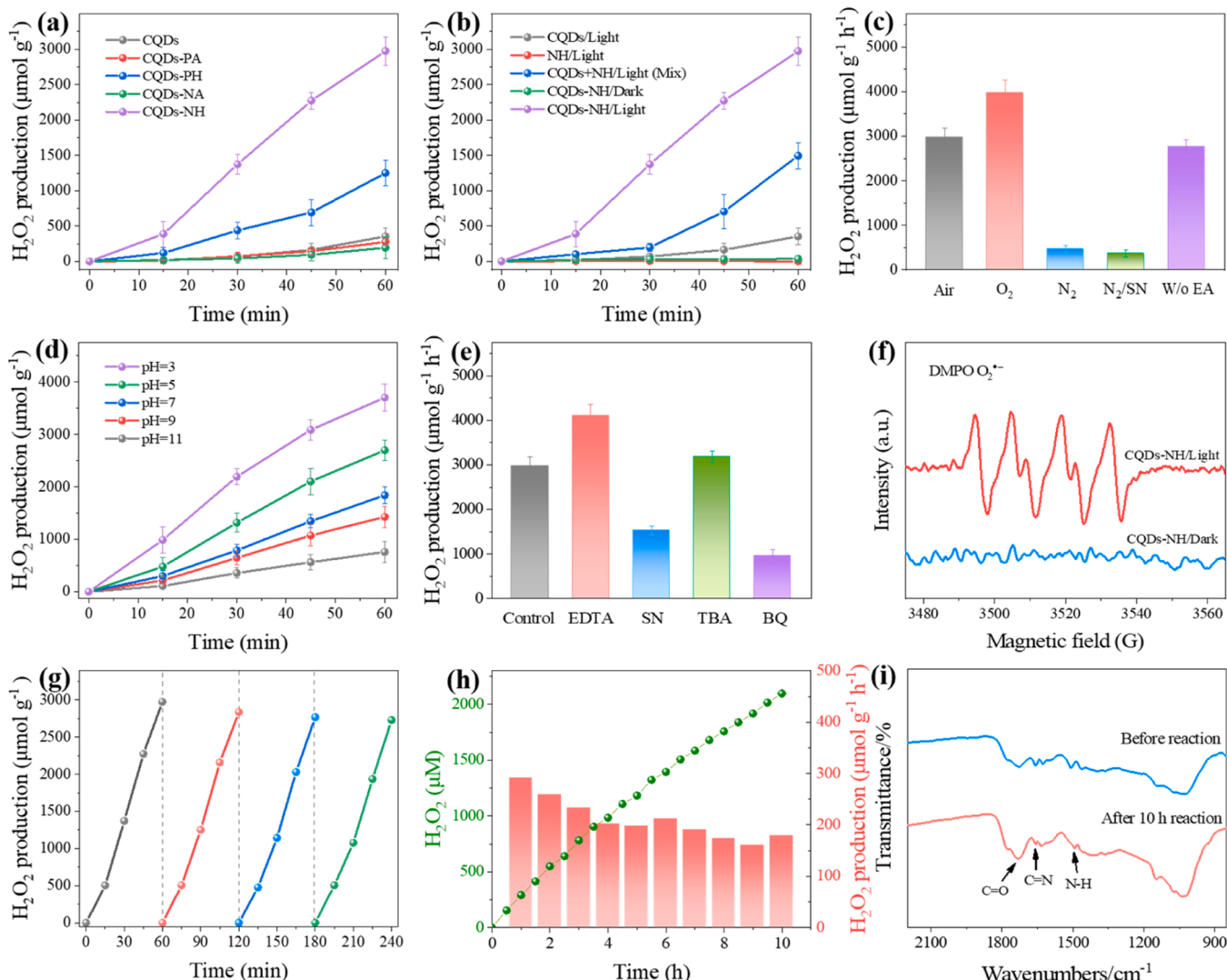


**Fig. 2.** (a) H<sub>2</sub>O<sub>2</sub> generation under light irradiation using different photocatalysts. (b) Time-dependent profiles of H<sub>2</sub>O<sub>2</sub> generation by CQDs, NH, CQDs-NH, and a physical mixture of CQDs and NH. (c) The H<sub>2</sub>O<sub>2</sub> generation of CQDs-NH at N<sub>2</sub>, O<sub>2</sub> and atmosphere with or without ethanol for 1 h. (d) pH-dependent H<sub>2</sub>O<sub>2</sub> generation rate of CQDs-NH for 1 h. (e) Quenching experiments. (f) EPR spectra of O<sub>2</sub><sup>·-</sup>. (g) Cyclic test for H<sub>2</sub>O<sub>2</sub> generation over CQDs-NH. (h) H<sub>2</sub>O<sub>2</sub> concentration profile of CQDs-NH over the 10-hour test; (i) FT-IR spectra of recycled CQDs-NH.

samples suggest that the carbonyl functional group titration on the CQDs surface does not affect the defect structure of the carbon matrix. XRD spectra (Fig. S2) of all samples show a broad peak at 19.5°, which corresponds to the (002) plane of graphitic carbon [21]. The FT-IR spectra (Fig. 1g) demonstrate that the C=O bond vibrational peak in CQDs derivatives at 1725 cm<sup>-1</sup> is significantly weaker compared to CQDs, with a new peak at 1660 cm<sup>-1</sup> attributed to the formation of the C=N bond [46]. Additionally, CQDs-PH and CQDs-NH exhibit a distinct peak around 1500 cm<sup>-1</sup>, corresponding to the vibrational peak of the -N-H bond [47]. XPS spectra (Fig. 1h) further confirm the successful functionalization, with N1s elemental peaks appearing at 397.0 eV in CQDs derivatives compared to CQDs. High-resolution N1s spectra (Fig. 1i-l) reveal peaks at 401.7, 400.4, and 399.5 eV, corresponding to N-H, C-N, and C=N bonds, respectively [48]. CQDs-PH and CQDs-NH, unlike CQDs-PA and CQDs-NA, show peaks at 401.7 eV for the N-H bond, indicative of sec-ammonia in PH and NH ligands. These results confirm successful reactions of PA, PH, NA, and NH with carbonyl groups on CQDs surface via Schiff-base condensation.

### 3.2. Photocatalytic production of H<sub>2</sub>O<sub>2</sub>

The photocatalytic activities of the samples were assessed through H<sub>2</sub>O<sub>2</sub> generation in a 10% ethanol solution (as the electron sacrifier) under light irradiation (Fig. 2a). Compared to CQDs, which yielded 354 μmol g<sup>-1</sup> h<sup>-1</sup> of H<sub>2</sub>O<sub>2</sub>, CQDs-PA and CQDs-NA showed decreased yields at 275 and 194 μmol g<sup>-1</sup> h<sup>-1</sup>, respectively. This reduction was attributed to the unfavorable PA and NA modification that disrupted CQDs' electronic structures and inhibit photogenerated electron-hole pair separation. Consequently, the H<sub>2</sub>O<sub>2</sub> generation was prohibited. In contrast, CQDs-PH and CQDs-NH exhibited a significant increase in the H<sub>2</sub>O<sub>2</sub> yields, with CQDs-NH demonstrating the highest activity at 2974 μmol g<sup>-1</sup> h<sup>-1</sup>, attaining an 8.4-fold increase compared to CQDs and a solar-to-chemical conversion efficiency of 0.23% (Text S4). The impact of varying NH dosages on H<sub>2</sub>O<sub>2</sub> production during the synthesis of CQDs-NH was investigated, as shown in Fig. S3. As NH dosage increased from 0 to 1 g (with increments of 0, 0.1, 0.25, 0.5, and 1.0 g), the H<sub>2</sub>O<sub>2</sub> yields correspondingly rose to 354, 1173, 2316, 2974, and 3081 μmol, respectively. These results indicate that the augmentation in NH molecules on CQD surface expanded the active sites available for the interaction between CQDs-NH and O<sub>2</sub>, thereby enhancing the H<sub>2</sub>O<sub>2</sub> production yield. However, the increase in H<sub>2</sub>O<sub>2</sub> production became marginal with NH doses beyond 0.5 g. This phenomenon suggests a saturation point due to the finite number of carbonyl groups on CQD surface, which limits further attachment of NH molecules. Consequently, for optimal catalyst efficiency, a dosage of 0.5 g of NH was identified as the most effective for further experiments. Further investigation of CQDs-NH's photocatalytic activity under varying conditions in Fig. 2b showed that NH alone produced negligible H<sub>2</sub>O<sub>2</sub>, confirming its lack of intrinsic photocatalytic ability. However, a physical mixture of CQDs and NH (CQDs+NH/Light (Mix)) yielded a significant increase in H<sub>2</sub>O<sub>2</sub> production (1494 μmol g<sup>-1</sup> h<sup>-1</sup>) compared to CQDs alone. This is potentially due to early-stage reaction forming CQDs-NH via Schiff-base condensation, as the kinetics start to raise after 30 min during the photocatalytic reaction. Additionally, CQDs-NH produced no H<sub>2</sub>O<sub>2</sub> in the absence of light, indicating that photogenerated electrons are crucial in the H<sub>2</sub>O<sub>2</sub> production.

The introduction of O<sub>2</sub> into the reaction system markedly increased H<sub>2</sub>O<sub>2</sub> generation from 2974 to 3975 μmol g<sup>-1</sup> h<sup>-1</sup> (Fig. 2c), whereas purging the system with N<sub>2</sub> to remove dissolved oxygen significantly reduced the yield to 465 μmol g<sup>-1</sup> h<sup>-1</sup>. These results underscore the vital role of dissolved oxygen in the photocatalytic production of H<sub>2</sub>O<sub>2</sub> by CQDs-NH. Additionally, with sufficient N<sub>2</sub> to eliminate the dissolved oxygen and adding silver nitrate as the electron acceptor, a modest amount of H<sub>2</sub>O<sub>2</sub> (366 μmol g<sup>-1</sup> h<sup>-1</sup>) was still generated. This suggests that a small amount of H<sub>2</sub>O could be directly oxidized by the holes in CQDs-NH, leading to the generation of H<sub>2</sub>O<sub>2</sub> during the photocatalytic

process. Notably, CQDs-NH still achieved a substantial H<sub>2</sub>O<sub>2</sub> yield of 2764 μmol g<sup>-1</sup> h<sup>-1</sup> even without the presence of the electron donor (ethanol), which is not only superior to most of the reported metal-free photocatalysts under pure water, but also to most of the catalysts with sacrificial agents (Table S1). The effect of initial pH on H<sub>2</sub>O<sub>2</sub> production performance was also explored in Fig. 2d, and a lower pH substantially increased the yield, reaching 3702 μmol g<sup>-1</sup> h<sup>-1</sup> at pH 3. This indicates that acidic conditions favor the photocatalytic proton-coupled electron transfer reaction for H<sub>2</sub>O<sub>2</sub> generation [41,49].

Trap quenching experiments were conducted using EDTA, silver nitrate (SN), tertiary butyl alcohol (TBA), and p-benzoquinone (BQ) as scavengers for holes (h<sup>+</sup>), electrons (e<sup>-</sup>), hydroxyl radicals (•OH), and superoxide anions (O<sub>2</sub><sup>•-</sup>), respectively, to identify the active species (Fig. 2e). The increased H<sub>2</sub>O<sub>2</sub> concentration in the EDTA solution was due to the consumption of oxidative holes which facilitated the electron-hole separation-H<sub>2</sub>O<sub>2</sub> generation decreased in the SN solution compared to the control experiment, highlighting the significant role of photoelectrons in H<sub>2</sub>O<sub>2</sub> production. The unchanged H<sub>2</sub>O<sub>2</sub> concentration in the TBA solution suggests that hydroxyl radicals are not the reactive species for H<sub>2</sub>O<sub>2</sub> generation via radical coupling. The reduced H<sub>2</sub>O<sub>2</sub> production in the presence of BQ, although still notable, suggests that superoxide anions are an important intermediate in H<sub>2</sub>O<sub>2</sub> production via a single-electron reaction, which was further reduced to H<sub>2</sub>O<sub>2</sub> generation via accepting another electron. Electron paramagnetic resonance (EPR) was employed to further confirm the presence of superoxide anions, as evidenced by sextuplet peaks corresponding to DMPO-O<sub>2</sub><sup>•-</sup> adducts in the CQDs-NH solution under light irradiation (Fig. 2f). Based on these findings, the proposed photocatalytic H<sub>2</sub>O<sub>2</sub> generation route by CQDs-NH is illustrated in Eqs. (3–5).



The reusability of CQDs-NH for H<sub>2</sub>O<sub>2</sub> production was assessed through four consecutive tests under visible light irradiation. CQDs-NH maintained stable photocatalytic performance, with the fourth run attaining a H<sub>2</sub>O<sub>2</sub> production rate of 2729 μmol g<sup>-1</sup> h<sup>-1</sup> (Fig. 2g). Long-term H<sub>2</sub>O<sub>2</sub> production performance was also evaluated, showing a gradual increase in accumulated H<sub>2</sub>O<sub>2</sub> concentration over 10 hours of light exposure, reaching 2096 μM (Fig. 2h). The efficiency of H<sub>2</sub>O<sub>2</sub> production decreased over time, possibly due to the reduced concentration of dissolved oxygen and ethanol depletion. Additionally, prolonged light exposure may have caused corrosion of active sites on CQDs-NH by the oxidative intermediate. This is supported by the weakened vibrational peaks of C=N and N-H bonds in FT-IR spectra after 10 hours, compared to the initial CQDs-NH (Fig. 2i).

### 3.3. Mechanism on the enhanced performance

Fig. 3a presents the UV-Vis absorption property of CQDs and their derivatives. All samples exhibit a pronounced absorption peak at 285 nm, which corresponds to the n-π\* transition in the C=O band and the π-π\* transition in the C=C band. In comparison with CQDs, the absorption edge of the CQDs derivatives is to the longer wavelength, accompanied by a broader shoulder peak at 370 nm due to the n-π\* transition of the C=N bond [46]. This indicates that the introduction of the four ligands (PA, PH, NA, and NH) all enhances the light absorption capabilities of CQDs. To estimate the band gap energy of these photocatalysts, UV-vis data were analyzed using the Kubelka-Munk function, and linear extrapolation was applied to the Tauc plot. As depicted in Fig. 3a (inset), band gaps (E<sub>g</sub>) of CQDs, CQDs-PA, CQDs-NA, CQDs-PH, and CQDs-NH are 3.92, 2.97, 2.94, 2.93, and 2.88 eV, respectively. The conduction band (CB) positions of the samples were further estimated from the Mott-Schottky diagram. As illustrated in Fig. 3b, the positive

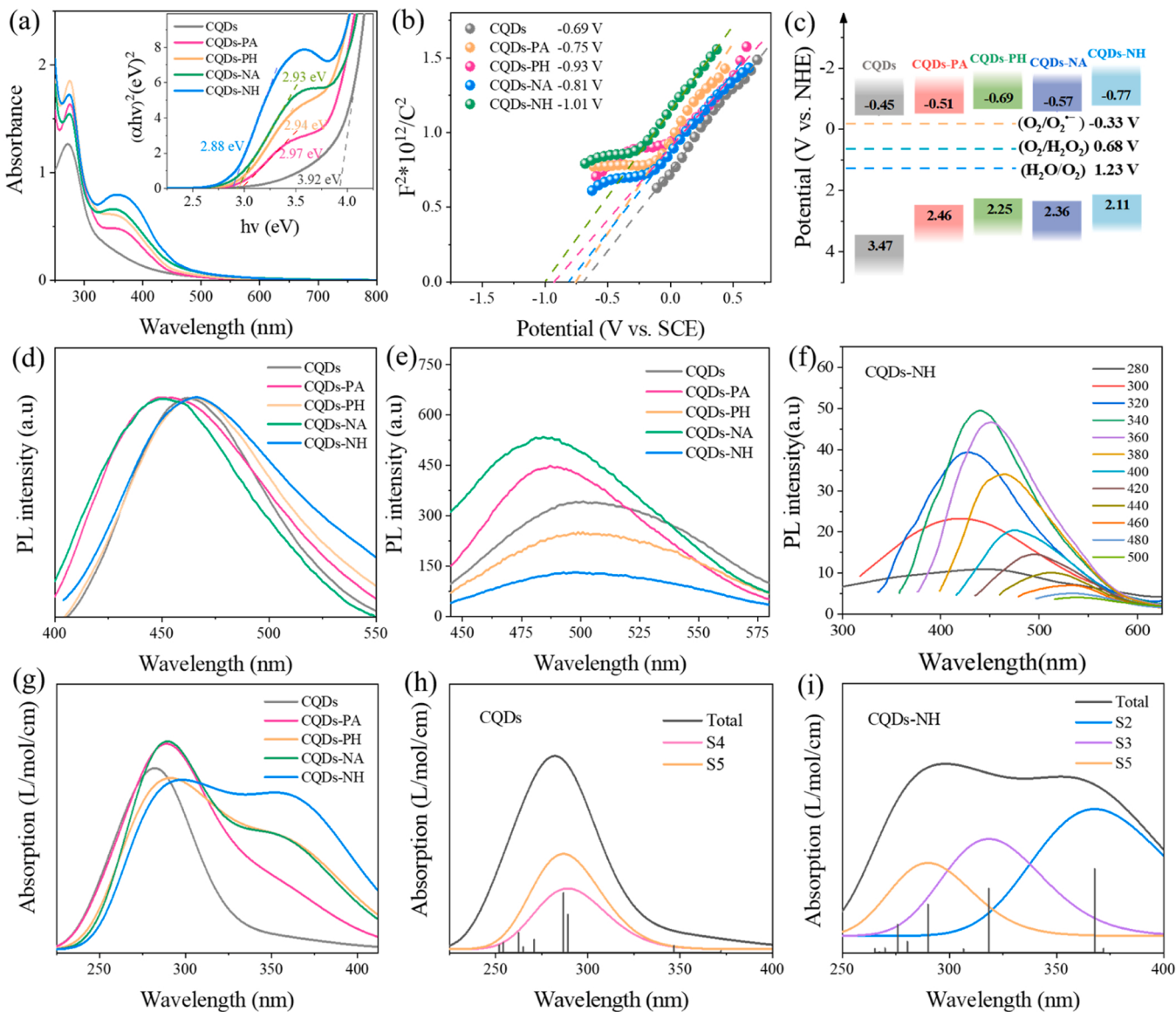


**Fig. 3.** (a) UV-vis absorption spectra (inset: the corresponding tauc plot), (b) Mott-Schottky plots, (c) schematic illustration of the band structures, (d) normalized PL emission spectra, (e) steady PL spectra at 420 nm for CQDs and derivatives. (f) PL emission spectra of CQDs-NH under excitation with light of different wavelengths. (g) Theoretical UV-vis spectrum of CQDs and CQDs-derivatives. Theoretically UV-vis spectral decomposition diagram of (h) CQDs and (i) CQDs-NH.

slope of the tangent line confirms that the synthesized CQDs and their derivatives are n-type semiconductors. The CB values of CQDs, CQDs-PA, CQDs-NA, CQDs-PH, and CQDs-NH are determined to be  $-0.69$ ,  $-0.75$ ,  $-0.93$ ,  $-0.81$ , and  $-1.01$  V vs SCE, respectively. The energy level diagrams of the samples can be deduced using the equation  $ENHE = E_{SCE} + 0.24$  and  $E_{VB} = E_{CB} + E_g$ . Fig. 3c illustrates the impact of ligand introduction on CQDs, specifically indicating an upward shift in their energy band positions and a concurrent reduction in the band gap. Notably, CQDs-NH has the smallest band gap, which is advantageous for the generation of photogenerated electrons and enhances photocatalytic activity. Additionally, the sufficiently negative CB of CQDs and their derivatives favors photocatalytic ORR thermodynamically. Moreover, the VB position of CQDs and their derivatives may allow photogenerated holes to oxidize  $H_2O$ , producing hydrogen protons and  $O_2$  which potentially contributed to the production of hydrogen peroxide [31].

Compared to CQDs, the photoluminescence (PL) emission peaks of CQDs-PA and CQDs-NA (Fig. 3d) exhibit a slight blue shift, potentially due to the introduction of ligands on the CQDs surface. Fig. 3e presents the steady PL spectra of CQDs and their derivatives under optical

excitation at 420 nm. Notably, the photoluminescence intensity of CQDs-PA and CQDs-NA is significantly enhanced compared to that of CQDs. Conversely, the PL intensity of CQDs-PH and CQDs-NH is reduced, suggesting that the introduction of PA and NA inhibits the separation of electron-hole pairs, while PH and NH promote the charge carriers' separation [50]. The PL emission spectra of CQDs and CQDs-NH, under various excitation wavelengths ranging from 280 to 500 nm, were also examined (Fig. S4, Fig. 3f). Both CQDs and CQDs-NH exhibit excitation-dependent photoluminescence, characterized by the red-shifting of photoluminescence emission peaks with increasing excitation wavelength. Moreover, the overall decrease in fluorescence intensity in CQDs-NH compared to CQDs suggests a reduction in the recombination rate of photogenerated electron-hole pairs, which is favorable for the separation of photogenerated carriers and thereby enhances photocatalytic activity.

To investigate the impact of surface state changes in CQDs on their photocatalytic activity, we developed a series of CQDs models. These models utilized graphene fragments with edges functionalized with PA, PH, NA, and NH to simulate various CQDs derivatives. The first five

excited states of both CQDs and CQDs-derivatives models were calculated using the TD-DFT method at the CAM-B3LYP/6–311 g (d, p) level. Theoretical UV-Vis spectroscopy and electron-hole analyses were conducted using Multiwfn 3.8 software[43,52]. The theoretical UV-Vis spectra (Fig. 3g) reveal that all samples exhibit strong absorption at 285 nm. The introduction of the four ligands (PA, PH, NA, and NH) results in a broad shoulder peak at 370 nm, with CQDs-NH showing the highest absorbance value. This aligns with the trend observed in the experimentally obtained UV-vis absorption spectra, confirming the validity of our constructed models. To elucidate the contribution of individual excited states to the absorption peaks, the theoretical UV-Vis spectra were further fitted (Fig. 3h-i, Fig. S5). It was noted that the absorption peaks at 370 nm for CQDs-derivatives were predominantly due to transitions from S0 to S2 excited states. Specifically, the absorption peaks of CQDs, CQDs-PA, CQDs-NA, CQDs-PH, and CQDs-NH at 280 nm were mainly attributed to S0 → S5, S0 → S5, S0 → S4, S0 → S4, and S0 → S5 transitions, respectively.

To delve deeper into the direction of intramolecular charge transfer in CQDs and CQDs-derivatives within these excited states, we employed the Mulliken-like method for hole-electron analysis and inter-fragment charge transfer (IFCT) calculations (Fig. 4) [53]. In comparison with CQDs (S0 → S2), the D-index for CQDs-PA and CQDs-NA decreased to 0.594 and 0.390 Å, respectively, from the original 0.869 Å. This suggests that the introduction of PA and NA suppresses the separation of electron-hole pairs. In contrast, the electron-hole distribution plots for CQDs-PH and CQDs-NH show a dramatic alteration in electron-hole distribution upon the introduction of PH and NH. Electrons are transferred along the C=N-NH bonds towards the graphene fragments (Fragment 2), while the holes predominantly reside in the PH and NH groups. This results in a significant increase in the D-index, rising from 0.869 to 0.895 and 1.112 Å, respectively. IFCT analysis clearly demonstrates intramolecular charge transfer, with CQDs, CQDs-PA, and CQDs-NA all exhibiting electron transfer from fragment 2 to fragment 1, at amounts of 0.084, 0.073, and 0.042 e<sup>-</sup>, respectively. Conversely, in CQDs-PH and CQDs-NH, electrons transfer from fragment 1 to fragment 2. Notably, in the NH group, electrons (0.118 e<sup>-</sup>) are more prone to transfer from fragment 1 to fragment 2 along the C=N-NH bond than in the PH group (0.1 e<sup>-</sup>). This trend is consistent across other excited states as well (Fig. 4g, i, k, m, o, and Table S2), indicating that electron transfer along the C=N-NH bonds to the graphene fragments in the excited state promotes the separation of photoinduced electron-hole pairs.

Electrochemical measurements were conducted to further elucidate the mechanism of the increased H<sub>2</sub>O<sub>2</sub> generation upon molecular engineering. As depicted in Fig. 5a, the transient photocurrents of CQDs and their derivatives under periodic light irradiation were assessed. Compared to CQDs, the photocurrent amplitudes for CQDs-PA and CQDs-NA diminished, while those for CQDs-PH and CQDs-NH increased, with CQDs-NH exhibiting the highest photocurrent amplitude. This suggests that CQDs-NH can excite more electron-hole pairs, significantly boosting the current density, which aligns with its photocatalytic activity. Electrochemical impedance spectra (EIS) were recorded for all samples to investigate electronic conductivity within the catalysts. The Nyquist plots, displayed in Fig. 5b, were analyzed using the equivalent circuit depicted in the inset. The charge transfer resistances (R<sub>ct</sub>) for CQDs, CQDs-PA, CQDs-PH, CQDs-NA, and CQDs-NH are 18,110, 13,125, 9736, 13,311, and 9583 Ω, respectively. These findings reveal that the CQDs-NH catalyst exhibits the most rapid charge transfer kinetics compared to the other catalysts. The cyclic voltammetry (CV) response of CQDs and their derivatives is shown in Fig. 5c. CQDs-NH registered the highest current value, implying the strongest electron transfer capacity, consistent with the EIS results[54]. Electrochemical CV is frequently utilized to determine the HOMO and LUMO energy levels of organic semiconductors [55]. Fig. S7 presents the CV curves of CQDs and their derivatives in a 0.1 M TBAP acetonitrile electrolyte, with Ag/Ag<sup>+</sup> serving as the selected reference electrode. The φ<sub>ox</sub> and φ<sub>red</sub> values for CQDs and its derivatives were derived from Fig. S7.

Subsequently, the E<sub>g</sub> values of CQDs, CQDs-PA, CQDs-PH, CQDs-NA, and CQDs-NH were calculated using Eqs S4-S6, yielding E<sub>g</sub> of 3.37, 3.1, 2.86, 2.99, and 2.67 eV, respectively, as listed in Table S3. These findings demonstrate that CQDs-NH possesses the narrowest band gap, enhancing its suitability for photocatalytic reactions.

To evaluate the electrochemical kinetics of CQDs and CQDs-NH towards ORR, rotating ring-disc electrodes (RRDE) were employed to perform linear sweep voltammetry (LSV) at various rotational speeds (Fig. 5d, e). For CQDs-NH, both ring and disc current densities witness significant increases compared to CQDs. The average electron transfer number was calculated as 2.45 and 2.56 for CQDs and CQDs-NH, with average H<sub>2</sub>O<sub>2</sub> selectivity of 77.5% and 72.2%, respectively (Fig. 5f). These values indicate a propensity for both CQDs and CQDs-NH towards two-electron ORR for H<sub>2</sub>O<sub>2</sub> generation. The lower electron transfer number and higher H<sub>2</sub>O<sub>2</sub> selectivity of CQDs-NH suggest that the introduction of NH facilitates a more selective two-electron reduction pathway in ORR.

To elucidate the promoted H<sub>2</sub>O<sub>2</sub> production upon functionality engineering, DFT was utilized to calculate the density of states (DOS), the lowest unoccupied molecular orbital (LUMO), and the highest occupied molecular orbital (HOMO) of CQDs and their derivatives [51,56]. The HOMO and LUMO of CQDs derivatives underwent significant changes due to alterations in surface chemistry. As evident from Fig. 6a, b, and d, the HOMO of CQDs-PH and CQDs-NH is primarily localized on the PH and NH groups, respectively, and the LUMO predominantly resides in the graphitic domain of CQDs-PH and CQDs-NH (Fig. 6c, e). This suggests the electron transfer from PH and NH groups to the graphitic domain [57]. The DOS plots of CQDs and their derivatives indicate that the molecular orbitals near the HOMO and LUMO are primarily composed of p orbitals, with s orbitals contributing only to lower and higher energy levels. Notably, the HOMO energy levels of CQDs-PH and CQDs-NH are mainly derived from the p-orbitals of the PH and NH groups, indicating that the presence of these groups significantly elevates the HOMO energy levels. Fig. 6f demonstrates that CQDs-NH has the smallest energy gap, implying that the introduction of NH decreases the energy barrier for the generation of photogenerated carriers, thereby boosting photocatalytic activity.

To investigate the active functional site of CQDs-NH for binding oxygen molecules, we utilized the genmer module of the Molclus program to generate 20 initial candidate conformations [58]. These initial conformations were optimized using the XTB program, and their optimized structural energies were screened using the isomer model of the Molclus program. The top nine structures with the lowest energies were further refined using Gaussian 16 C.01 software at the B3LYP/6–311 g (d, p) level. Analysis of the first five optimized structures with the lowest energy revealed that oxygen was predominantly localized around the NH group. This indicates that the NH group possesses the strongest oxygen adsorption capacity compared to other active sites on CQDs-NH (Fig. S8). The structure with the lowest energy, depicted in Fig. 7a, shows the binding energy of CQDs-NH and an oxygen molecule to be -55.97 kJ/mol as per Eq. S1, suggesting a weak interaction between CQDs-NH and oxygen molecules. Hirschfeld partition (IGMH) analysis was employed to further determine the binding site and the nature of forces between CQDs-NH and oxygen molecules [59,60]. In the IGMH diagram, the colors of the isosurfaces indicate the types of interactions: blue for strong attraction (e.g., hydrogen bonding), green for weak attraction (e.g., van der Waals interaction), and red for strong repulsion (e.g., spatial site-blocking). Fig. 7b reveals significant an der Waals interactions between the PH group and oxygen molecules. Notably, the hydrogen atoms on the sec-ammonia contribute the most (42%) to the binding with oxygen molecules, and the blue isosurfaces at the junction of hydrogen atoms and oxygen molecules signify hydrogen bonding between them.

Previous studies on intramolecular charge transfer revealed that electrons in the NH group of CQDs-NH tend to transfer along the C=N-NH bond bridges to the graphite domains in the excited state, leading to

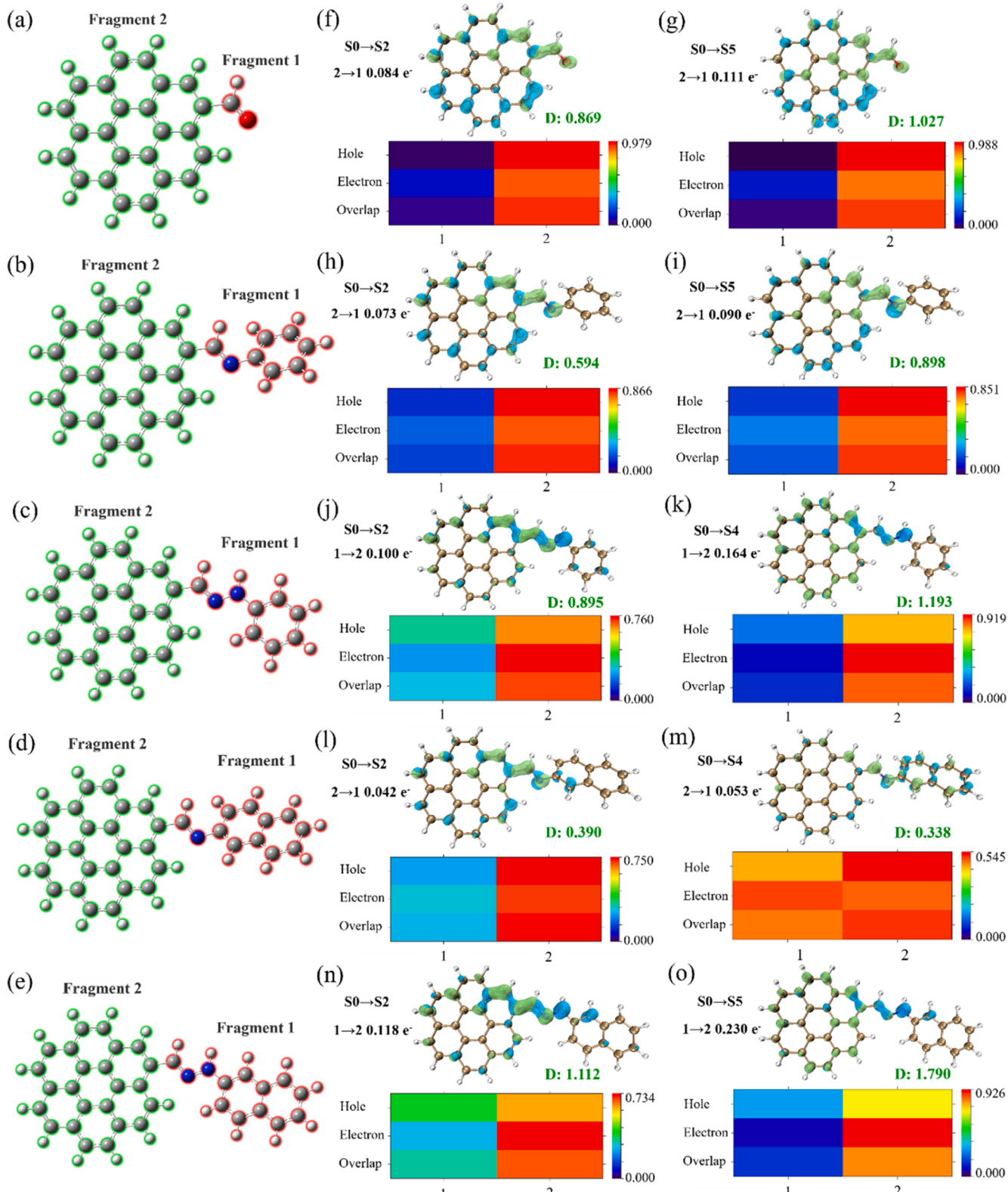


**Fig. 4.** Excitation properties of CQDs and CQDs-derivatives. The chemical structure (a) CQDs, (b) CQDs-PA, (c) CQDs-PH, (b) CQDs-NA, and (d) CQDs-NH (All models are divided into two fragments.). Electron-hole distribution and heat map of hole-electron composition of (f, g) CQDs, (h, i) CQDs-PA, (j, k) CQDs-PH, (l, m) CQDs-NA, (n, o) CQDs-NH in the excited state. The green and blue isosurfaces represent electron and hole distributions, respectively. (D: The centroid distance of electron and holes; 2 → 1: Fragment 2 transfers electrons to fragment 1.).

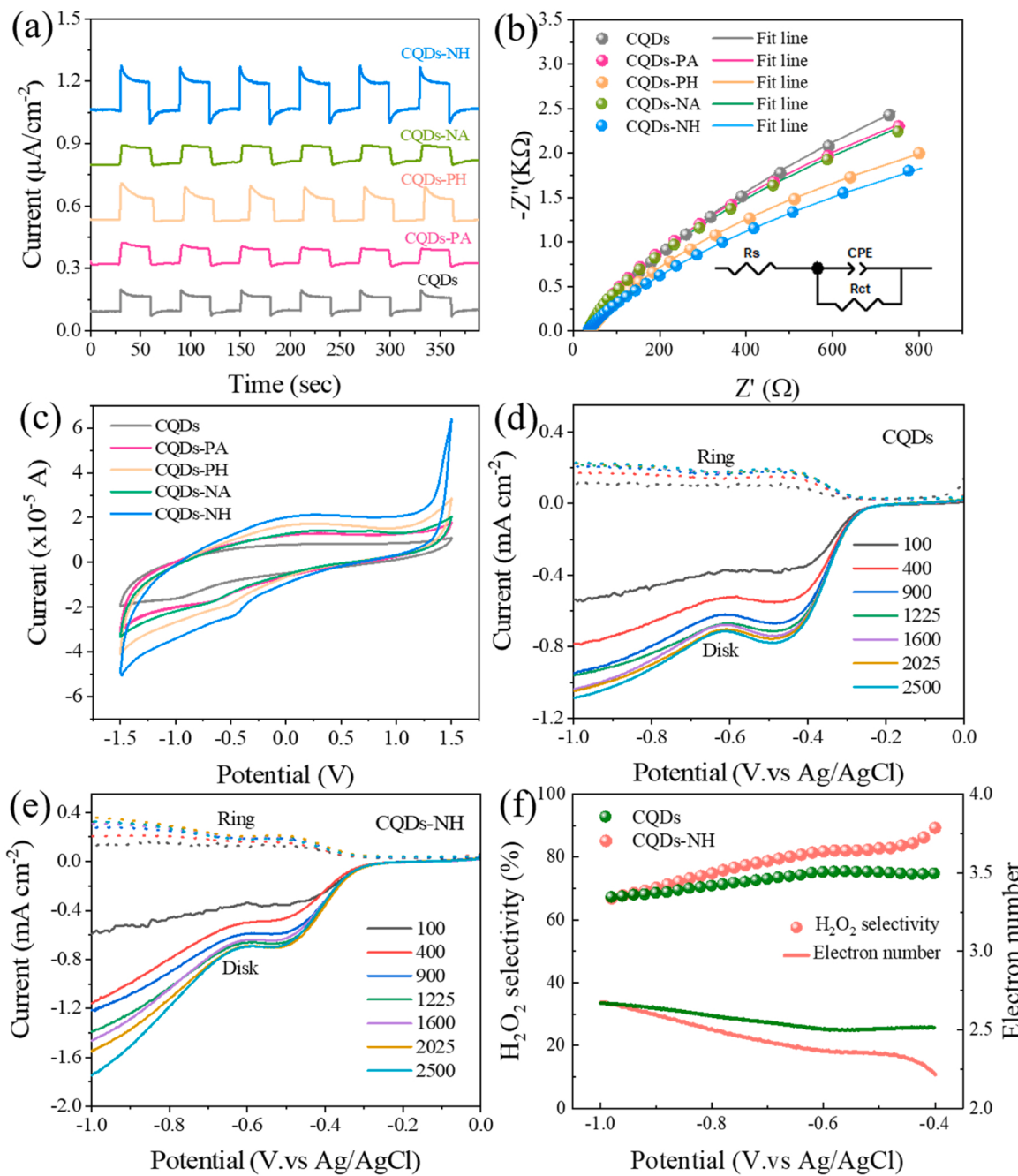


**Fig. 5.** (a) Photocurrent response, (b) EIS Nyquist plots under light irradiation, inset: An equivalent circuit impedance diagram. (c) CV curves of CQDs and CQDs-derivatives. LSV curve collected on RRDE of (d) CQDs and (e) CQDs-NH at different rotation speeds from 100 to 2500 rpm. (f) the calculated  $\text{H}_2\text{O}_2$  selectivity and electron transfer number at 1600 rpm as a function of the applied potential for CQDs and CQDs-NH.

holes surrounding the N-H bond region. Further investigation into the specific electron transfer in the NH group was conducted via charge density difference analysis. The charge density difference plots (Fig. 7c, d) show that the region of electron depletion is primarily concentrated at the N-H bond. These findings suggest that the N-H bond will be broken to yield hydrogen protons, while the presence of hydrogen bonding between hydrogen atoms and oxygen aids proton transfer, thereby promoting  $\text{H}_2\text{O}_2$  production. This also explains the efficient production of  $\text{H}_2\text{O}_2$  by CQDs-NH in the absence of a sacrificial agent. The free energy diagram for the oxygen reduction pathway towards  $\text{H}_2\text{O}_2$  production on different active sites in CQDs-NH, shown in Fig. 7e, indicates that the NH group has the lowest overpotential for  $\text{H}_2\text{O}_2$  formation, implying a heightened reactivity for  $\text{H}_2\text{O}_2$  production [61]. Moreover, in-situ

ATR-FTIR spectra (Fig. 7f, g) confirmed that the N-H bond content decreases under light exposure and gradually recovers in dark conditions. This suggests that the hydrogen atoms in the C=N-NH<sub>2</sub> moieties of the NH group can function as proton conductors, enabling rapid proton transfer and facilitating proton-coupled electron transfer to produce  $\text{H}_2\text{O}_2$ . Protons on the NH group can be replenished by nearby protons derived from ethanol and  $\text{H}_2\text{O}$ .

Based on these findings, Fig. 8 presents a proposed mechanism for  $\text{H}_2\text{O}_2$  generation by CQDs-NH under light illumination. Under light excitation, electrons and holes in CQDs-NH are separated and migrate to different polarized sites on CQDs. On one hand, the hole oxidizes ethanol (the hole sacrifier), producing hydrogen protons to participate in  $\text{H}_2\text{O}_2$  production. On the other hand, photogenerated electrons, transferred to

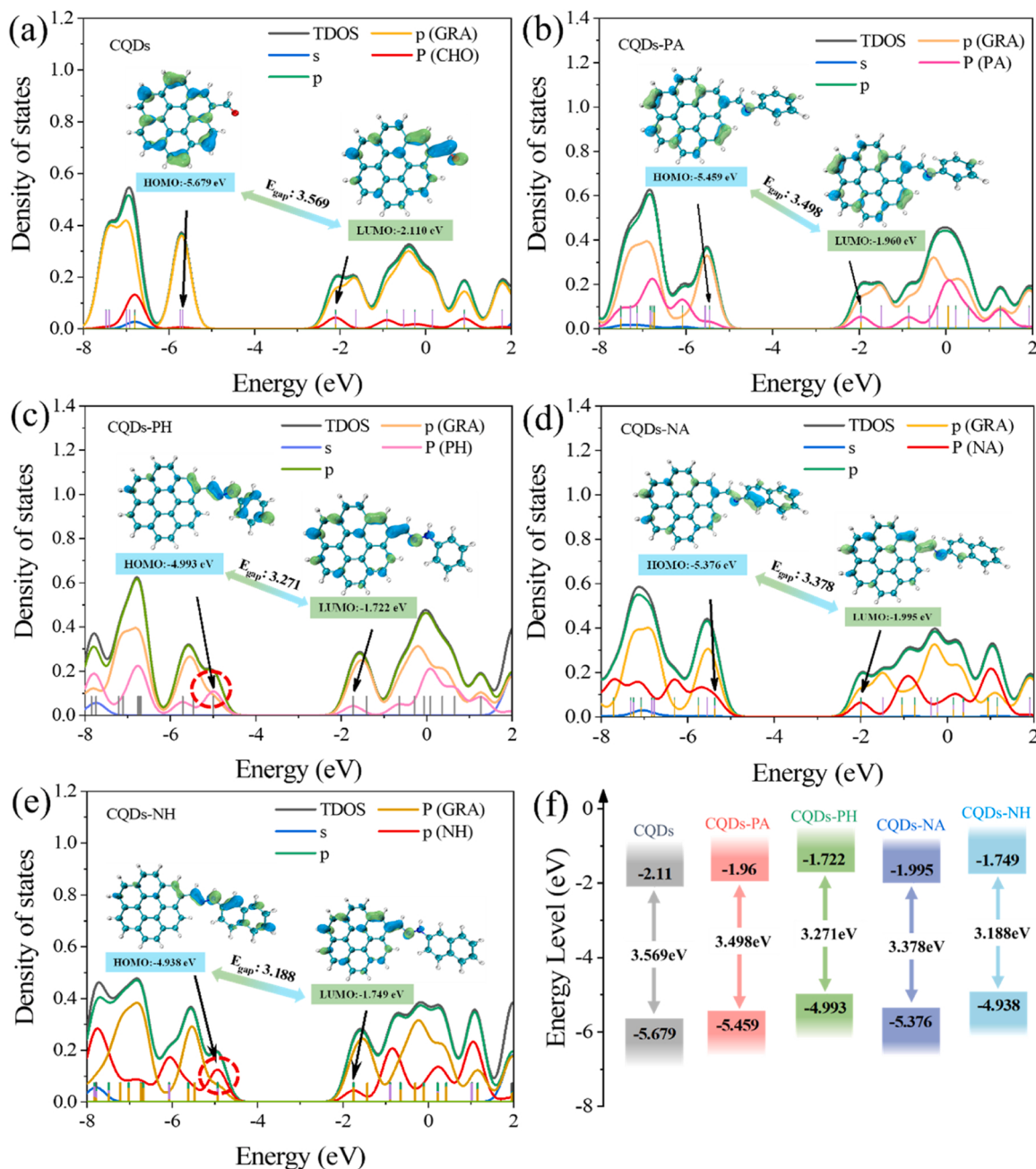


**Fig. 6.** Total DOS and PDOS and the HOMO and LUMO of (a) CQDs, (b) CQDs-PA, (c) CQDs-PH, (d) CQDs-NA and (e) CQDs-NH. (f) Schematic diagram of HOMO and LUMO for CQDs, CQDs-PA, CQDs-PH, CQDs-NA, and CQDs-NH.

the graphite domains via the C=N-NH- bridge, react with adsorbed oxygen to form superoxide anions ( $O_2^-$ ), which subsequently react with hydrogen protons to form  $H_2O_2$ . Furthermore, the ammonia hydrogen atom in the NH group serves as a proton conductor to facilitate proton-coupled electron transfer in the photocatalytic reduction of  $O_2$  toward  $H_2O_2$  production. Additionally, the hydrogen atom on the NH group can be replenished by protons generated through the hole oxidation of ethanol and  $H_2O$ .

#### 4. Conclusion

In conclusion, this study developed efficient and metal-free CQDs-NH photocatalysts through surface chemical modification based on a Schiff-base condensation reaction. The introduction of the NH group significantly enhanced the photocatalytic  $H_2O_2$  generation, with CQDs-

NH showing an 8.4 times higher yield than pristine CQDs. This improvement was attributed to enhanced light absorption, carrier separation and transfer, selectivity for two-electron ORR, and enhanced oxygen adsorption. Experimental and theoretical analyses provided insights into the photocatalytic mechanism, highlighting the role of the C=N-NH- group in promoting proton-coupled electron transfer and efficient  $H_2O_2$  production. This research lays the groundwork for future studies on engineering of state-of-the-art quantum materials for efficient  $H_2O_2$  generation leveraging solar light.

#### CRediT authorship contribution statement

**Xuliang Zhang:** Investigation, Formal analysis. **Shaobin Wang:** Writing – review & editing, Conceptualization. **Xiaoguang Duan:** Writing – review & editing, Supervision, Methodology,

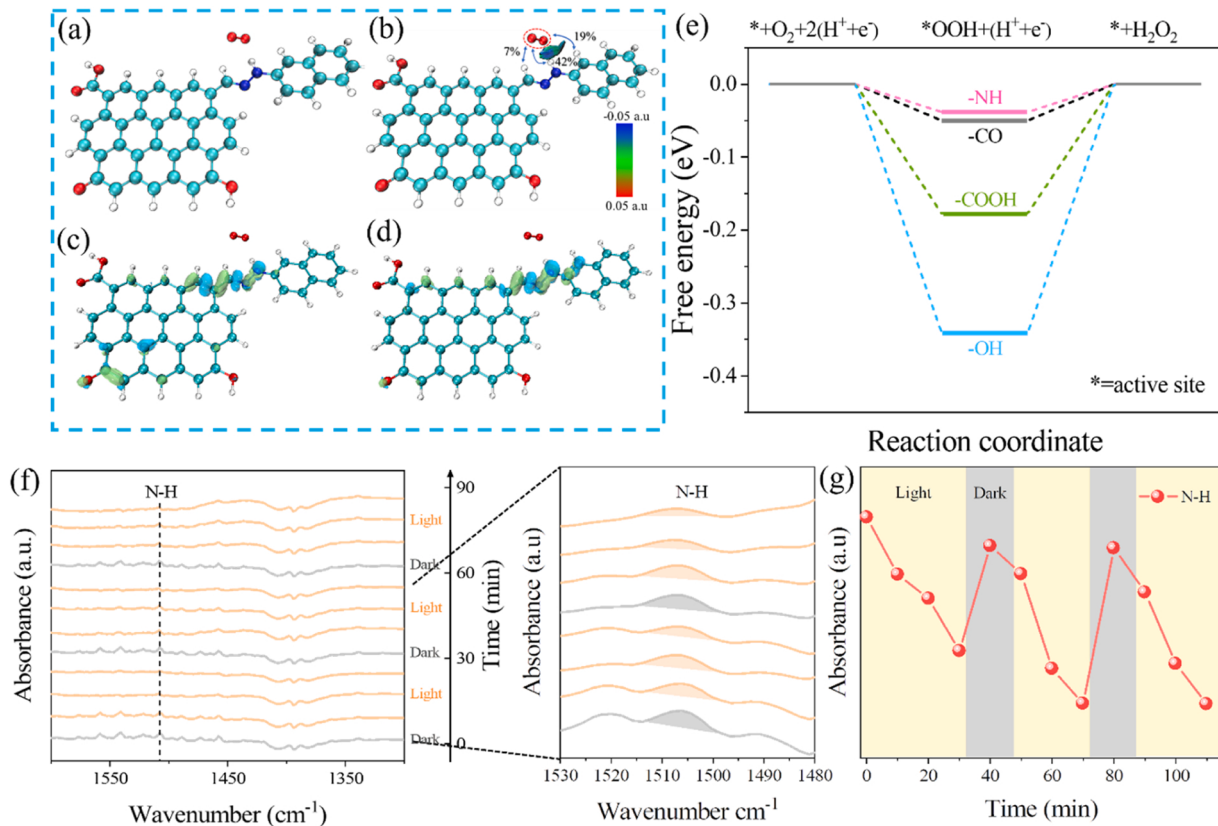


**Fig. 7.** (a) Optimized structures of CQDs-NH for oxygen adsorption. (b) The IGMH isosurface color map analyses for CQDs-NH/O<sub>2</sub>. The charge density difference ( $\rho_{TS}$ ) in the (c) S0 → S2 and (d) S0 → S5 excited state. (blue iso-surface: electron depletion region, green iso-surface: electron accumulation region) (e) The free energy diagram of CQDs-NH. (f) In-situ ATR-FTIR spectroscopy of oxygen adsorption on CQDs-NH. (g) The change in the corresponding absorbance of N-H groups in in-situ ATR-FTIR spectroscopy of CQDs-NH with a periodic light irradiation for 10 min.

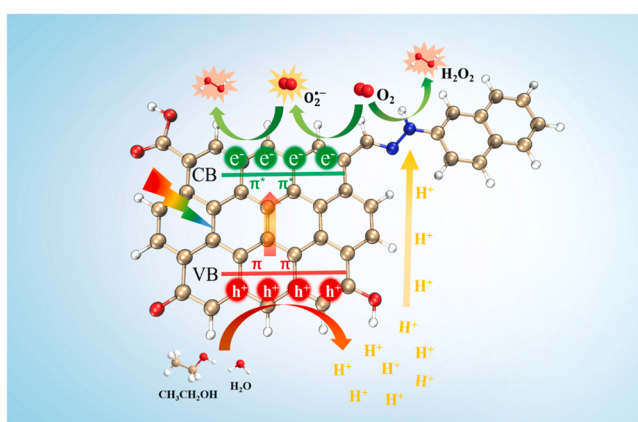


**Fig. 8.** Proposed mechanism for enhanced H<sub>2</sub>O<sub>2</sub> production over chemically modified CQDs.

Conceptualization. **Wenyuan Han:** Writing – original draft, Investigation, Formal analysis, Conceptualization. **Hao Zhang:** Investigation, Formal analysis. **Degang Li:** Writing – original draft, Validation, Investigation. **Wenwu Qin:** Writing – review & editing, Visualization, Supervision, Project administration, Conceptualization.

#### Declaration of Competing Interest

The authors declare that they have no known competing financial interests or personal relationships that could have appeared to influence the work reported in this paper.

#### Data availability

Data will be made available on request.

#### Acknowledgements

This work was partially supported by the Australian Research Council via Discovery Early Career Award Research Scheme (DE210100253) and National Computational Infrastructure (NCMAS-2023-78), the National Natural Science Foundation of China (22002074).

#### Appendix A. Supporting information

Supplementary data associated with this article can be found in the online version at doi:10.1016/j.apcatb.2024.123918.

#### References

- [1] M. Michele, F. Paolo, P. Maurizio, The rise of hydrogen peroxide as the main product by metal-free catalysis in oxygen reductions, *Adv. Mater.* 31 (2019) 1802920.
- [2] S.C. Perry, D. Pangotra, L. Vieira, L.I. Csepei, V. Sieber, L. Wang, C.P. De Leon, F. C. Walsh, Electrochemical synthesis of hydrogen peroxide from water and oxygen, *Nat. Rev. Chem.* 3 (2019) 442–458.
- [3] Q. Wu, J. Cao, X. Wang, Y. Liu, Y. Zhao, H. Wang, Y. Liu, H. Huang, F. Liao, M. Shao, A metal-free photocatalyst for highly efficient hydrogen peroxide photoproduction in real seawater, *Nat. Commun.* 12 (2021) 483.
- [4] J.Z. A, C.Y. B, J.L. A, Y.Z. B, B.Z. A, Y.H.H. A, M.L. A, Modulation of Lewis acid-base sites for efficient photocatalytic H<sub>2</sub>O<sub>2</sub> production over potassium intercalated tri-s-triazine materials-ScienceDirect, *Appl. Catal. B Environ.* 277 (2020) 119225.
- [5] V.R. Choudhary, A.G.G. And, S.D. Sansare, Nonhazardous direct oxidation of hydrogen to hydrogen peroxide using a novel membrane catalyst, *Angew. Chem. Int. Ed.* 113 (2001) 1826–1829.

- [6] M. Jose, Gema Campos-Martin, Blanco-Brieva, L. Jose, G. Fierro, Hydrogen peroxide synthesis: an outlook beyond the anthraquinone process, *Angew. Chem. Int. Ed.* 45 (2006) 6962–6984.
- [7] S. Yang, A. Verdaguera-Casadevall, L. Arnarson, L. Silvioli, V. Colic, R. Frydendal, J. Rossmeisl, I. Chorkendorff, I.E. Stephens, Toward the decentralized electrochemical production of H<sub>2</sub>O<sub>2</sub>: a focus on the catalysis, *ACS Catal.* 8 (2018) 4064–4081.
- [8] S. Kolagatla, P. Subramanian, A. Schechter, Simultaneous mapping of oxygen reduction activity and hydrogen peroxide generation on electrocatalytic surfaces, *ChemSusChem* 12 (2019) 2708–2714.
- [9] W. Yu, C. Hu, L. Bai, N. Tian, Y. Zhang, H. Huang, Photocatalytic hydrogen peroxide evolution: what is the most effective strategy? *Nano Energy* 104 (2022) 107906.
- [10] H. Hou, X. Zeng, X. Zhang, Production of hydrogen peroxide by photocatalytic processes, *Angew. Chem. Int. Ed.* 59 (2020) 17356–17376.
- [11] L. Chen, C. Chen, Z. Yang, S. Li, C. Chu, B. Chen, Simultaneously tuning band structure and oxygen reduction pathway toward high-efficient photocatalytic hydrogen peroxide production using cyano-rich graphitic carbon nitride, *Adv. Funct. Mater.* 31 (2021) 2105731.
- [12] H. Song, L. Wei, L. Chen, H. Zhang, J. Su, Photocatalytic production of hydrogen peroxide over modified semiconductor materials: a minireview, *Top. Catal.* 63 (2020) 895–912.
- [13] S. Zhao, T. Guo, X. Li, T. Xu, B. Yang, X. Zhao, Carbon nanotubes covalent combined with graphitic carbon nitride for photocatalytic hydrogen peroxide production under visible light, *Appl. Catal. B Environ.* 224 (2018) 725–732.
- [14] L. Cheng, H. Zhang, X. Li, J. Fan, Q. Xiang, Carbon-graphitic carbon nitride hybrids for heterogeneous photocatalysis, *Small* 17 (2021) 2005231.
- [15] L. Liu, M.-Y. Gao, H. Yang, X. Wang, X. Li, A.I. Cooper, Linear conjugated polymers for solar-driven hydrogen peroxide production: the importance of catalyst stability, *J. Am. Chem. Soc.* 143 (2021) 19287–19293.
- [16] W. Zhao, P. Yan, B. Li, M. Bahri, L. Liu, X. Zhou, R. Clowes, N.D. Browning, Y. Wu, J.W. Ward, Accelerated synthesis and discovery of covalent organic framework photocatalysts for hydrogen peroxide production, *J. Am. Chem. Soc.* 144 (2022) 9902–9909.
- [17] S.Y. Lim, W. Shen, Z. Gao, Carbon quantum dots and their applications, *Chem. Soc. Rev.* 44 (2015) 362–381.
- [18] P. Devi, S. Saini, K.-H. Kim, The advanced role of carbon quantum dots in nanomedical applications, *Biosens. Bioelectron.* 141 (2019) 111158.
- [19] R. Das, R. Bandyopadhyay, P. Pramanik, Carbon quantum dots from natural resource: a review, *Mater. Today Chem.* 8 (2018) 96–109.
- [20] W. Han, D. Li, X. Hu, Photocatalytic activation of peroxyxonosulfate by carbon quantum dots: rational regulation of surface functionality and computational insights, *Materials Today, Chemistry* 30 (2023) 101546.
- [21] W. Han, D. Li, M. Zhang, X. Hu, S. Wang, Photocatalytic activation of peroxyxonosulfate by surface-tailored carbon quantum dots, *J. Hazard. Mater.* 395 (2020) 122695.
- [22] A. Mei, Z. Xu, X. Wang, Y. Liu, J. Chen, J. Fan, Q. Shi, Photocatalytic materials modified with carbon quantum dots for the degradation of organic pollutants under visible light: a review, *Environ. Res.* 214 (2022) 114160.
- [23] K.-H. Ye, Z. Wang, J. Gu, S. Xiao, Y. Yuan, Y. Zhu, Y. Zhang, W. Mai, S. Yang, Carbon quantum dots as a visible light sensitizer to significantly increase the solar water splitting performance of bismuth vanadate photoanodes, *Energy Environ. Sci.* 10 (2017) 772–779.
- [24] Y. Dong, Q. Han, Q. Hu, C. Xu, C. Dong, Y. Peng, Y. Ding, Y. Lan, Carbon quantum dots enriching molecular nickel polyoxometalate over CdS semiconductor for photocatalytic water splitting, *Appl. Catal. B Environ.* 293 (2021), 120214.
- [25] H. Li, Y. Deng, Y. Liu, X. Zeng, D. Wiley, J. Huang, Carbon quantum dots and carbon layer double protected cuprous oxide for efficient visible light CO<sub>2</sub> reduction, *Chem. Commun.* 55 (2019) 4419–4422.
- [26] Z. Zhao, H. Zhang, X. Song, Y. Shi, D. Si, H. Li, C. Hao, Insight into the CO<sub>2</sub> photoreduction mechanism over 9-hydroxyphenyl-1-one (HPHN) carbon quantum dots, *J. Energy Chem.* 52 (2021) 269–276.
- [27] Z. Liu, W. Hou, H. Guo, Z. Wang, L. Wang, M. Wu, Functional group modulation in carbon quantum dots for accelerating photocatalytic CO<sub>2</sub> reduction, *ACS Appl. Mater. Interfaces* 15 (2023) 33868–33877.
- [28] T. Fei, L. Yu, Z. Liu, Y. Song, F. Xu, Z. Mo, C. Liu, J. Deng, H. Ji, M. Cheng, Graphene quantum dots modified flower like Bi<sub>2</sub>WO<sub>6</sub> for enhanced photocatalytic nitrogen fixation, *J. Colloid Interface Sci.* 557 (2019) 498–505.
- [29] Y. Hu, Z.L. Zhao, R. Ahmad, M. Harb, L. Cavallo, L.M. Azofra, X. Zhang, A bifunctional catalyst based on a carbon quantum dots/mesoporous SrTiO<sub>3</sub> heterostructure for cascade photoelectrochemical nitrogen reduction, *J. Mater. Chem. A* 10 (2022) 12713–12721.
- [30] P. Ma, X. Zhang, C. Wang, Z. Wang, K. Wang, Y. Feng, J. Wang, Y. Zhai, J. Deng, L. Wang, Band alignment of homojunction by anchoring CN quantum dots on g-C<sub>3</sub>N<sub>4</sub> (0D/2D) enhance photocatalytic hydrogen peroxide evolution, *Appl. Catal. B Environ.* 300 (2022), 120736.
- [31] J. Shi, Y. Luo, T. Yang, H. Wang, C. Ju, K. Pu, J. Shi, T. Zhao, J. Xue, Y. Li, Enhanced nonsacrificial photocatalytic generation of hydrogen peroxide under visible light using modified graphitic carbon nitride with doped phosphorus and loaded carbon quantum dots: constructing electron transfer channel, *J. Colloid Interface Sci.* 628 (2022) 259–272.
- [32] X. Zhou, F. Yan, A. Lyubartsev, B. Shen, J. Zhai, J.C. Conesa, N. Hedin, Efficient production of solar hydrogen peroxide using piezoelectric polarization and photoinduced charge transfer of nanopiezoelectrics sensitized by carbon quantum dots, *Adv. Sci.* 9 (2022) 2105792.
- [33] C. Zhao, X. Wang, S. Ye, J. Liu, Graphene quantum dots-modified resorcinol-formaldehyde resin for efficient hydrogen peroxide production, *Sol. RRL* 6 (2022) 2200427.
- [34] Y. Li, Y. Zhao, H. Nie, K. Wei, J. Cao, H. Huang, M. Shao, Y. Liu, Z. Kang, Interface photo-charge kinetics regulation by carbon dots for efficient hydrogen peroxide production, *J. Mater. Chem. A* 9 (2021) 515–522.
- [35] M.K. Barman, A. Patra, Current status and prospects on chemical structure driven photoluminescence behaviour of carbon dots, *J. Photochem. Photobiol. C Photochem. Rev.* 37 (2018) 1–22.
- [36] Z. Zhu, X. Li, M. Luo, M. Chen, W. Chen, P. Yang, X. Zhou, Synthesis of carbon dots with high photocatalytic reactivity by tailoring heteroatom doping, *J. Colloid Interface Sci.* 605 (2022) 330–341.
- [37] S. Miao, K. Liang, J. Zhu, B. Yang, D. Zhao, B. Kong, Hetero-atom-doped carbon dots: doping strategies, properties and applications, *Nano Today* 33 (2020) 100879.
- [38] T. Song, X. Zhang, P. Yang, Bifunctional nitrogen-doped carbon dots in g-C<sub>3</sub>N<sub>4</sub>/WO<sub>x</sub> heterojunction for enhanced photocatalytic water-splitting performance, *Langmuir* 37 (2021) 4236–4247.
- [39] B. Zhang, G. An, J. Chen, H. Guo, L. Wang, Surface state engineering of carbon dot/carbon nanotube heterojunctions for boosting oxygen reduction performance, *J. Colloid Interface Sci.* 637 (2023) 173–181.
- [40] M. Gu, D.-Y. Lee, J. Mun, D. Kim, H. i Cho, B. Kim, W. Kim, G. Lee, B.-S. Kim, H. i Kim, Solar-to-hydrogen peroxide conversion of photocatalytic carbon dots with anthraquinone: unveiling the dual role of surface functionalities, *Appl. Catal. B Environ.* 312 (2022) 121379.
- [41] Y. Yan, J. Chen, N. Li, J. Tian, K. Li, J. Jiang, J. Liu, Q. Tian, P. Chen, Systematic bandgap engineering of graphene quantum dots and applications for photocatalytic water splitting and CO<sub>2</sub> reduction, *ACS Nano* 12 (2018) 3523–3532.
- [42] H. Xiaopeng, H. Xiaojing, S. Fahui, Z. Jincai, Z. Lizhi, Facet-dependent Cr (VI) adsorption of hematite nanocrystals, *Environ. Sci. Technol.* 50 (2016) 1964–1972.
- [43] T. Lu, F. Chen, Multiwfns: a multifunctional wavefunction analyzer, *J. Comput. Chem.* 33 (2012) 580–592.
- [44] S. Chen, T. Luo, K. Chen, Y. Lin, J. Fu, K. Liu, C. Cai, Q. Wang, H. Li, X. Li, Chemical identification of catalytically active sites on oxygen-doped carbon nanosheet to decipher the high activity for electro-synthesis hydrogen peroxide, *Angew. Chem.* 133 (2021) 16743–16750.
- [45] M. Fan, Z. Wang, K. Sun, A. Wang, Y. Zhao, Q. Yuan, R. Wang, J. Raj, J. Wu, J. Jiang, N-B-OH site-activated graphene quantum dots for boosting electrochemical hydrogen peroxide production, *Adv. Mater.* 35 (2023) 2209086.
- [46] W. Han, D. Li, Y. Kong, W. Liu, W. Qin, S. Wang, X. Duan, High-performance photocatalytic peroxyxonosulfate activation by carbon quantum dots via precise surface chemistry regulation: insight into the structure-function relations, *J. Colloid Interface Sci.* 646 (2023) 633–648.
- [47] M.J. Krysmann, A. Kelarakis, P. Dallas, E.P. Giannelis, Formation mechanism of carbogenic nanoparticles with dual photoluminescence emission, *J. Am. Chem. Soc.* 134 (2012) 747–750.
- [48] T. Liu, G. Yin, Z. Song, J. Yu, X. Yong, B. Zhang, L. Ai, S. Lu, Solid-State luminescence in self-assembled chlorosalicylaldehyde-modified carbon dots, *ACS Mater. Lett.* 5 (2023) 846–853.
- [49] G.-h Moon, W. Kim, A.D. Bokare, N.-e Sung, W. Choi, Solar production of H<sub>2</sub>O<sub>2</sub> on reduced graphene oxide-TiO<sub>2</sub> hybrid photocatalysts consisting of earth-abundant elements only, *Energy Environ. Sci.* 7 (2014) 4023–4028.
- [50] K. Wang, M. Zhang, D. Li, L. Liu, Z. Shao, X. Li, H. Arandiyani, S. Liu, Ternary BaCaZrTi perovskite oxide piezocatalysts dancing for efficient hydrogen peroxide generation, *Nano Energy* 98 (2022) 107251.
- [51] W. Liu, P. Wang, J. Chen, X. Gao, H. Che, B. Liu, Y. Ao, Unraveling the mechanism on ultrahigh efficiency photocatalytic H<sub>2</sub>O<sub>2</sub> generation for dual-heteroatom incorporated polymeric carbon nitride, *Adv. Funct. Mater.* 32 (2022) 2205119.
- [52] Z. Liu, T. Lu, Q. Chen, An sp-hybridized all-carboatomic ring, cyclo [18] carbon: electronic structure, electronic spectrum, and optical nonlinearity, *Carbon* 165 (2020) 461–467.
- [53] H. Che, J. Wang, P. Wang, Y. Ao, J. Chen, X. Gao, F. Zhu, B. Liu, Simultaneously achieving fast intramolecular charge transfer and mass transport in holey d-π-a organic conjugated polymers for highly efficient photocatalytic pollutant degradation, *JACS Au* 3 (2023) 1424–1434.
- [54] Z. Zhang, L. Huang, S. Cheng, C. Jiang, Y. Wang, M.I.L.-125 (Ti)-derived, COOH functionalized TiO<sub>2</sub> grafted molecularly imprinted polymers for photoelectrochemical sensing of ofloxacin, *Sens. Actuators B Chem.* 343 (2021) 130119.
- [55] X. Li, S. Luo, H. Sun, H.H.-Y. Sung, H. Yu, T. Liu, Y. Xiao, F. Bai, M. Pan, X. Lu, Medium band-gap non-fullerene acceptors based on a benzothiophene donor moiety enabling high-performance indoor organic photovoltaics, *Energy Environ. Sci.* 14 (2021) 4555–4563.
- [56] Z. Liu, X. Wang, T. Lu, A. Yuan, X. Yan, Potential optical molecular switch: lithium@ cyclo [18] carbon complex transforming between two stable configurations, *Carbon* 187 (2022) 78–85.
- [57] X. Tang, L.-S. Cui, H.-C. Li, A.J. Gillett, F. Auras, Y.-K. Qu, C. Zhong, S.T. Jones, Z.-Q. Jiang, R.H. Friend, Highly efficient luminescence from space-confined charge-transfer emitters, *Nat. Mater.* 19 (2020) 1332–1338.
- [58] B. Zhao, H. Ma, H. Jia, M. Zheng, K. Xu, R. Yu, S. Qu, Z.A. Tan, Triphenylamine-derived solid-state emissive carbon dots for multicolor high-efficiency electroluminescent light-emitting diodes, *Angew. Chem.* 135 (2023) e202301651.

- [59] T. Le Bahers, C. Adamo, I. Ciofini, A qualitative index of spatial extent in charge-transfer excitations, *J. Chem. Theory Comput.* 7 (2011) 2498–2506.
- [60] Y. Chen, F. Zhao, B. Zeng, Fabrication of surface molecularly imprinted electrochemical sensor for the sensitive quantification of chlortetracycline with ionic liquid and MWCNT improving performance, *Talanta* 239 (2022) 123130.
- [61] C. Chen, X.T. Wang, J.H. Zhong, J. Liu, G.I. Waterhouse, Z.Q. Liu, Epitaxially grown heterostructured  $\text{SrMn}_3\text{O}_{6-x}\text{-SrMnO}_3$  with high-valence  $\text{Mn}^{3+/\text{4}+}$  for improved oxygen reduction catalysis, *Angew. Chem.* 133 (2021) 22214–22221.